The effect of degassing and volatile exsolution on the composition of a trachybasaltic melt decompressed at slow and fast rates

Silvio Mollo [a], Francesco Vetere [b], Harald Beherens [c],
Vanni Tecchiato [a], Antonio Langone [d], Piergiorgio Scarlato [e], Diego Perugini [b]

[a] Dipartimento di Scienze della Terra, Sapienza-Università di Roma, P.le Aldo Moro 5, 00185 Rome, Italy
[b] Dipartimento di Fisica e Geologia, Università di Perugia, Piazza Università 1, 06100 Perugia, Italy
[c] Institute of Mineralogy, Leibniz University of Hannover, Callinstr. 3, 30167 Hannover, Germany
[d] C.N.R.-Istituto di Geoscienze e Georisorse, UOS Pavia, Via Ferrata 1, 27100 Pavia, Italy
[e] Istituto Nazionale di Geofisica e Vulcanologia, Via di Vigna Murata 605, 00143 Rome, Italy

ARTICLE INFO

ABSTRACT

It is widely accepted that, for the correct interpretation of bulk rock compositions, degassing process controlling both loss of magmatic volatiles and significant changes in the contents of volatile chemical species must be considered. The continuous degassing experiments presented in this study attempt to determine the absolute and relative change in abundances of volatile components in the melt at shallow levels, simulating what might occur during slow and fast ascent of magma from depth without crystallization. We performed disequilibrium decompression experiments using as starting melt a bubble-free but volatile-bearing trachybasalt. The charges were isothermally decompressed at 1,150 °C from 400 MPa down to 50 MPa at rates of 0.01 MPa/s and 1 MPa/s. Results demonstrate that degassing of 1 wt% H_2O of initial volatile content in the melt is not enough to induce melt compositional changes as well as H_2O supersaturation in the trachybasaltic melt. In contrast, the minimum H_2O threshold to observe Cl, B, and Li devolatilization corresponds to 3 wt% H_2O and volatile supersaturation is attained at the fast decompression rate of 1 MPa/s. An increase of CO_2 up to 0.3 wt% do not change the partitioning behaviour of these chemical species between vapor and trachybasaltic melt. Moreover, CO_2 degassing is less efficient with respect to H_2O transfer from the melt into the vapor phase. As a consequence, the trachybasaltic melt is preferentially supersaturated in CO_2 with decreasing pressure. Disequilibrium degassing does not change the bulk oxidation state of the melt.

Keywords: magma degassing; volatile exsolution; disequilibrium degassing; decompression; magma ascent; trachybasalt.

INTRODUCTION

Magma degassing and associated gas emissions in volcanic areas are generally used as premonitory signals of changes in the eruptive style and/or magmatic activity (Duffell et al., 2003). Although surface gases are often assumed to represent part of the volatile budget of the magma at depth (Symonds et al., 1994), the degassing process is controlled by volatile solubility and vapor-melt partitioning as a function of temperature, pressure, and composition of melt and vapor (Gardner et al., 2006).

In this framework, experimental studies dealing with magma decompression and degassing may help to

PM

elucidate the changes in the physicochemical state of magma during ascent and eruption to the surface (Stelling et al., 2008; Masotta et al., 2014; Fiege and Chichy, 2015). These studies focus on volcanic conduit regimes at relatively low pressures (≤500 MPa), representative of shallow depth degassing processes (≤20 km). The degassing path of magma is reproduced in laboratory by (1) single-step, (2) multi-step, and (3) continuous decompression (Brugger and Hammer, 2010; Nowak et al., 2011). The single-step method can be considered as the first attempt to simulate a natural scenario in which the entire ascent path is accomplished almost instantaneously within a few seconds; then, an annealing time is applied before quenching, despite the effect of annealing is implausible during volcanic eruptions and fast magma withdrawal. The multi-step method is a further experimental attempt to reproduce (but not entirely) a natural decompression mechanism by regular pressure drops followed by short-term annealing times until the experiment is quenched. Only in the most recent times, novel types of experimental devices allowed to faithfully simulate natural magma ascent conditions by continuous decompression experiments in which no severe pressure drops occur and the decompression rate is constant until the final quench pressure is reached (Brugger and Hammer, 2010; Nowak et al., 2011; Marxer et al., 2015; Preuss et al., 2016).

Magma compositional changes during decompression and volatile loss are frequently investigated in literature by ensuring excess of vapor along the entire decompression path and without modulating the decompression rate (Gardner et al., 2006). Additionally, data on vapor-melt elemental partitioning are obtained by isobaric experiments in which the melt approaches to equilibrium in a vapor-saturated system (Webster et al., 1989). In contrast, by continuous decompression experiments, it is now possible to explore the disequilibrium effects caused by rapid decompression of initially bubble-free melts that progressively degas with decreasing pressure (Lesne et al., 2011).

In this study, continuous decompression experiments have been designed to mimic disequilibrium degassing when variable concentrations of H_2O+CO_2 dissolved in the melt progressively exsolve as the pressure decreases from 400 MPa to 50 MPa. The experiments were conducted at both slow (0.01 MPa/s) and fast (1 MPa/s) decompression rates using as starting composition a natural trachybasalt from Mt. Etna volcano (Sicily, Italy) kept at the superliquidus temperature of 1,150 °C. In terms of major and trace elements as well as volatile contents and iron speciation, the final degassed glasses were compared with the original undegassed trachybasalt. Results from this comparison allow to quantify the compositional

changes in the melt and coexisting vapor when the state of the system shifts from vapor-undersaturated to vapor-saturated.

METHODS
Starting material and experiments

The starting material is a natural trachybasaltic lava that was erupted at Mt. Etna volcano during the intermediate to final activity of the Ellittico eruptive centre (since 15 ka). The lava flow is associated with lateral eruptions at 2,000 m a.s.l. on the flank of the volcanic edifice (Lanzafame et al., 2013 and references therein).

According to melt inclusion data and hygrometric estimates tracking the behaviour of volatiles at Mt. Etna volcano (Spilliaert et al., 2006; Collins et al., 2009; Armienti et al., 2013; Mollo et al., 2015a; Perinelli et al., 2016), the following range of volatiles contents were adjusted: 1.0-3.0 wt% H_2O and 0.0-0.1-0.3 wt% CO_2 (Table 1S). The powdered rock, deionised water and silver oxalate ($Ag_2C_2O_4$) as source of CO_2, were loaded in $Au_{80}Pd_{20}$ capsules. Details on capsules preparation are given in Vetere et al. (2014). The generated melts are volatiles undersaturated at the initial experimental pressure of 400 MPa corresponding to magmas residing at about 12 km depth.

Isothermal decompression experiments were performed at 1,150 °C in an internally heated pressure vessel (IHPV) at the Institute for Mineralogy, Leibniz University of Hannover (Germany). The use of Ar-H_2 mixture as a pressure medium provided the possibility to adjust the required fH_2 in the vessel (cf. Berndt et al., 2002). The experiments were conducted at the QFM (quartz–fayalite–magnetite) buffer, corresponding to the reducing conditions measured for the natural trachybasalt (Lanzafame et al., 2013). Within the sample capsule, the hydrogen fugacity was affected by permeation of hydrogen through the capsule walls driven by different fH_2 between the pressure medium and the capsule interior. This in turn, controls the fugacity of oxygen inside the capsule through the equilibrium reaction of water formation ($H_2+1/2O_2 \rightarrow H_2O$). At the beginning of the experiment the hydrogen fugacity inside the capsule is in disequilibrium with the pressure medium. The initial annealing period is devoted to homogenize the system with respect to the redox state. Permeation rates through the capsule wall and diffusion in the melt is sufficient to achieve equilibrium within 48 h at 1,150 °C (Botcharnikov et al., 2008). After pre-equilibration, the charges were isothermally decompressed from 400 MPa down to 50 MPa at rates of 0.01 MPa/s and 1 MPa/s. It is worth stressing that the decompression rates of 0.01 MPa/s and 1 MPa/s translate to magma ascent velocities of 0.02 and 2.86 m/s, respectively, that are in agreement with those

measured for eruptions at Mt. Etna volcano (Aloisi et al., 2006; Armienti et al., 2013; Mollo et al., 2015b) and other volcanic systems worldwide (Rutherford and Hill, 1993; Demouchy et al., 2006; Rutherford, 2008; Toramaru et al., 2008; Hildner et al., 2011; Gonnermann and Manga, 2012). Samples were rapidly quenched when reaching the final pressure. Quench rate was in the order of 200 °C/s (Berndt et al., 2002).

To determine the mole fraction of H_2O and CO_2 in the vapor phase exsolved during decompression, after the runs, the capsules were weighed, frozen by placing them into a bath of liquid nitrogen and then punctured with a needle. After warming to room temperature, capsules were weighed again to determine the mass of CO_2 in the fluid, then placed in a drying oven for some minutes and finally weighed to measure the mass of lost H_2O. The capsule weight was periodically checked until the weight remained constant.

In order to obtain an undegassed reference glass with composition unaffected by the effect of decompression rate and volatile exsolution, the powdered rock containing 1 wt% H_2O was equilibrated isobarically and isothermally at 400 MPa and 1,150 °C for 48 h, and then rapidly quenched (Table 1S). The recovered run products were mounted in epoxy and polished thin sections were produced for spectroscopic and compositional analyses.

Analytical techniques

Images of the experimental glasses were collected at the HPHT Laboratory of Experimental Volcanology and Geophysics of the INGV using the backscattered electron (BSE) mode of a field emission gun-scanning electron microscopy (FE-SEM) Jeol 6500F equipped with an energy-dispersive spectrometer (EDS) detector.

Microprobe analyses of experimental glasses were carried out at the same laboratory on a Jeol-JXA8200 electronic probe micro analysis (EPMA) equipped with five spectrometers (Table 1S). The analyses were conducted using an accelerating voltage of 15 kV and a beam current of 10 nA. A slightly defocused electron beam with a size of 10 μm was used with a counting time of 5 s on background and 15 s on peak. The following standards have been adopted for the various chemical elements: jadeite (Si and Na), corundum (Al), forsterite (Mg), andradite (Fe), rutile (Ti), orthoclase (K), barite (Ba), apatite (P), spessartine (Mn) and chromite (Cr). Sodium and potassium were analysed first to prevent alkali migration effects. Analyses of Cl, S, and F, were performed separately using a beam current of 80 nA, a defocused electron beam of 20 μm, and a counting time of 200 s (Cl and S) or 400 s (F). The beam was blanked regularly with the Faraday cup to minimize volatile losses during analysis and counts were collected in 20 s intervals

by 10 iterations for Cl and S, and 20 iterations for F. Variations in the wavelength of S Kα X-ray as a function of its oxidation state in glasses were taken into account during analysis through standards with known S valence states: $BaSO_4$ (barite) was used for calibration of the S^{6+} Kα peak, and FeS (pyrrhotite) for S^{2-}. Detection limits for Cl, S, and F were 0.01, 0.01, and 0.02 wt%, respectively. The precision of the microprobe was measured through the analysis of well-characterized glasses and minerals. Analysing these test materials as unknowns ensured data quality. Based on counting statistics, analytical uncertainties relative to their reported concentrations indicate that precision was better than 5% for all cations.

Trace element analyses of experimental glasses were conducted at the CNR-IGG in Pavia (Italy) with a LA-ICP-MS (Laser Ablation-Inductively Coupled Plasma-Mass Spectrometry) (Table 1S). The chosen trace elements were representative of the most important geochemical groups: rare earth elements (REE), high field strength elements (HFSE), large-ion lithophile elements (LILE), light lithophile elements (LLE) and transition elements (TE). The laser source used for the analyses consists of a Q-switched Nd:YAG laser (Brilliant, Quantel), with a fundamental emission in the near-IR region (1064 nm) which is converted into 266 nm by two harmonic generators. Using mirrors, the laser beam is carried into a petrographic microscope, focused above the sample, and then projected onto it. Operating conditions were: RF power 800-900 W, cooling gas 12.08 l min⁻¹, sample gas 0.9-1.1 l min⁻¹, auxiliary gas 1.00 l min⁻¹ and carrier gas 0.9-1.1 l min⁻¹. The spot size was 20 μm, the total scan-time was about 700 ms, the settling time was about 340 ms, and hence the acquisition efficiency was estimated at about 50%. A typical analysis consisted of acquiring data for one minute on background and one minute on ablated sample. The mean integrated time for acquisition was about 0.9 s for each element. The ablated material was analysed with a single-collector double-focusing sector-field ICP-MS (Element, Finnigan Mat, Bremen, Germany). NIST - SRM 610 standard reference glass (National Institute of Standards and Technology, Standard Reference Material 610) was used as an external standard, whereas ^{29}Si was adopted as internal standard for glass analyses. In each analytical run the USGS reference sample BCR2 was analysed together with the unknowns for quality control. The precision of individual analyses varied depending upon a number of factors, e.g., properties of the elements and isotopes analysed as well as the sample homogeneity.

Ferrous-ferric ratios were determined at the Institute for Mineralogy, Leibniz University of Hannover (Germany) through a wet chemical micro-colorimetric method (Schuessler et al., 2008) (Table 1S). Glass chips of about 6 mg were dissolved in concentrated HF to which a solution

of ammonium vanadate in 5 M sulfuric acid was added. At these acidic conditions, the released ferrous iron reacts with V^{5+} forming V^{4+} and ferric iron. The reaction products are more stable with respect to oxidation in air than ferrous iron so that the initial redox state of the glass is preserved in the solution. After complete sample dissolution at room temperature, saturated hot boric acid (80 °C) is added to neutralize the excess HF and to bring eventually formed fluorides back into solution. Adjusting the solution to a pH value of 5 using an ammonium acetate buffer regenerates Fe^{2+}. For the colorimetric analysis, 2,2' bipyridyl was added which forms a stable complex with Fe^{2+}. To quantify the concentration of this complex, the characteristic absorption band at 523 nm is applied. Measurements of concentrations of ferrous Fe and total Fe were made on the same solution before and after adding solid hydroxylamine hydrochloride. This reducing agent converts all ferric Fe into the ferrous state. Since both Fe^{2+} and total Fe determination were done on the same solution, uncertainties in the Fe^{2+}/Fe_{tot} ratios arise mainly from the absorbance measurements for which a 1 cm transmission cell in an UV/VIS spectrometer Shimadzu UV 1800 was used. Calibration of the spectrometric technique was made by measuring ferrous ammonium sulphate solutions with different known Fe^{2+} concentrations. Schuessler et al. (2008) estimated the uncertainty on Fe^{2+}/Fe_{tot} ratios to be 0.03.

Fourier Transform Infrared Spectroscopy (FTIR) analyses were carried out at the Institute for Mineralogy, Leibniz University of Hannover (Germany) to determine the concentrations of H_2O and CO_2 dissolved in the glasses (Table 1S). Absorption spectra were collected in the mid-infrared (MIR) using an FTIR spectrometer Bruker IFS88 coupled with an IR-ScopeII microscope (operation conditions: globar light source, KBr beamsplitter, MCT detector). Spectral resolution was 2 cm^{-1}. For each spectrum, 50-100 scans were collected. The spot size applied in analyses was typically 50×50 μm. The analysed area was checked optically before FTIR measurements to avoid any possible fluid bubbles. To minimize the contribution of atmospheric CO_2 to the MIR spectra, the sample stage of the IR microscope was shielded and purged with dry air. Doubly polished glass plates of about 60-110 μm thickness were prepared from the experimental products for IR spectroscopy. The thickness of each section was measured with a digital micrometre (Mitutoyo; precision ±2 μm). The concentration of dissolved volatile species in the investigated glasses was calculated using the Beer-Lambert law (e.g., Stolper, 1982):

$$C_i = \frac{100 \times M_i \times A_j}{d \times \rho \times \varepsilon} \qquad (1)$$

where C_i is the concentration of species i in wt%, M_i is the molecular weight of the species, A_j is the absorbance (peak height) of band j, d is the thickness of the section, ρ is the density in g l^{-1} and ε is the absorption coefficient in l mol^{-1} cm^{-1} (see data in Table 1S). Densities of glasses were calculated using the empirical equation of Ohlhorst et al. (2001) for basaltic compositions. A linear baseline was fitted to the 3,550 cm^{-1} band used for the determination of the water content. To separate the carbonate bands from superimposed overtones of lattice vibrations, a spectrum of a carbonate-free glass scaled to same thickness was subtracted from the sample spectra. The absorbance of the band at 1,430 cm^{-1} was used for quantifying the carbonate content. The absorption coefficients of 63±5 l mol^{-1}cm^{-1} (Dixon et al., 1995) and 170±18 l mol^{-1}cm^{-1} (Dixon and Pan, 1995) were applied to determine the total H_2O (3,530 cm^{-1}) and CO_3^{2-} (1,515-1,430 cm^{-1}), respectively.

RESULTS AND DISCUSSION
Bubble formation during melt decompression

Figure 1 shows some representative microphotographs of the decompression runs. At the sub-micrometre spatial resolution of FE-SEM analysis, minerals did not crystallize from the trachybasaltic melt. The staring material was kept at the superliquidus condition for 48 h and, consequently, all crystals in the trachybasalt dissolved over this time. The quenched glasses are almost homogenous in composition (see below), suggesting that dissolution was rapid and equilibrium was attained. The superliquidus conditions also assured that no crystals formed during the decompression experiments, likely favouring homogeneous bubble nucleation and growth (Fiege and Chichy, 2015).

Bubbles are ubiquitous in all the glasses testifying to volatile exsolution and degassing during decompression. In our experiments the formation of bubbles occurs irrespective of the decompression rate and/or the initial volatile content. In general, the size of bubbles ranges from a few micrometres up to about 300 μm. The mechanisms of bubble nucleation and growth as well as the analysis of bubble size distribution and bubble number density are beyond the scope of this study, but it is nevertheless striking that the maximum size of bubbles changes as a function of (1) the total volatile content and (2) the decompression rate (cf. Fiege et al., 2014). When the initial volatile content is 1 wt% H_2O+0.0 wt% CO_2, 1 wt% H_2O+0.1 wt% CO_2, and 1 wt% H_2O+0.3 wt% CO_2, respectively, the maximum bubble size increases from about 90 to 110 to 150 μm (at the slow decompression rate of 0.01 MPa/s) and from about 40 to 50 to 70 μm (at the fast decompression rate of 1 MPa/s). If instead the initial volatile content is 3 wt% H_2O+0.0 wt% CO_2, 3 wt% H_2O+0.1 wt% CO_2, and 3 wt% H_2O+0.3 wt% CO_2,
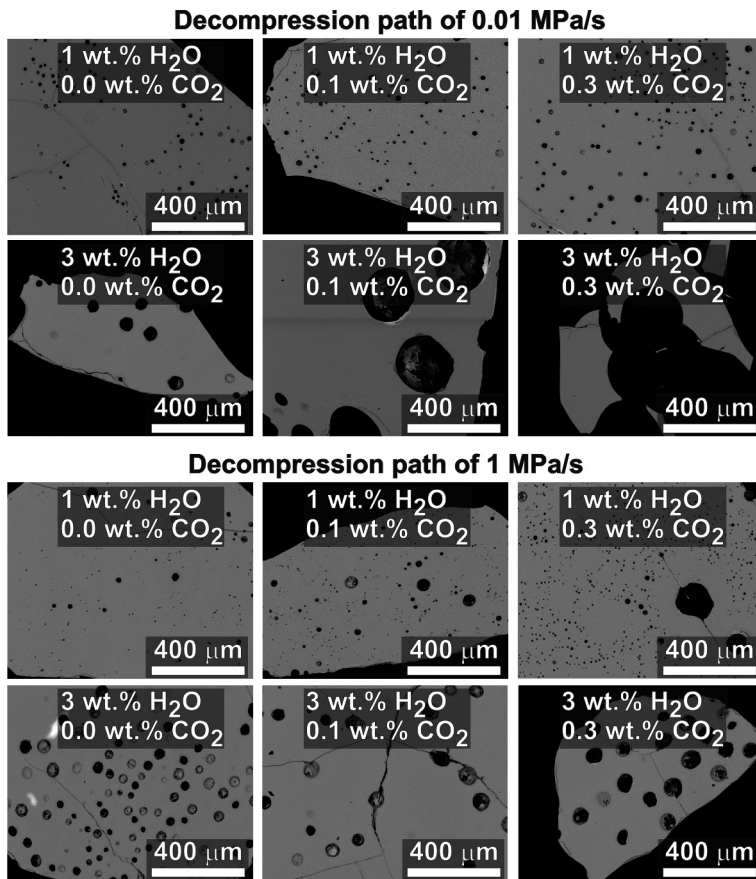
Decompression path of 0.01 MPa/s

Decompression path of 1 MPa/s

Figure 1. Representative microphotographs of the decompression runs. When the initial volatile content is 1 wt% H_2O+0.0 wt% CO_2, 1 wt% H_2O+0.1 wt% CO_2, and 1 wt% H_2O+0.3 wt% CO_2, respectively, the maximum bubble size increases from about 90 to 110 to 150 μm (at the slow decompression rate of 0.01 MPa/s) and from about 40 to 50 to 70 μm (at the fast decompression rate of 1 MPa/s). When the initial volatile content is 3 wt% H_2O+0.0 wt% CO_2, 3 wt% H_2O+0.1 wt% CO_2, and 3 wt% H_2O+0.3 wt% CO_2, respectively, the maximum bubble size increases from about 110 to 200 to 300 μm (at the slow decompression rate of 0.01 MPa/s) and from about 90 to 120 to 150 μm (at the fast decompression rate of 1 MPa/s).

respectively, the maximum bubble size increases from about 110 to 200 to 300 μm (at the slow decompression rate of 0.01 MPa/s) and from about 90 to 120 to 150 μm (at the fast decompression rate of 1 MPa/s).

It is also apparent from Figure 1 that the total amount of bubble increases with increasing decompression rate. This is particularly true for the decompression experiments containing 3 wt% H_2O in which bubble connectivity is more effective, especially for the coalescence of large-sized bubbles in the experiment decompressed at 0.01 MPa/s with 3 wt% H_2O+0.3 wt% CO_2 (Figure 1). Since the time allowed for bubble connection decreases as decompression rate increases, bubble coalescence tends to be limited or incomplete in fast decompression experiments (Burgisser and Gardner, 2004). On the other hand, the increase of the bubble size with increasing CO_2 contents may suggest the occurrence of an early nucleation event, as recorded by the largest vesicles for decompression path at 1 MPa/s (Blower et al., 2001). Moreover, with increasing decompression rate, the difference between gas pressure in the melt and the pressure at which bubble nucleation occurs (defined as the supersaturation pressure) is found to increase (e.g., Mangan and Sisson, 2000). Supersaturation is typically produced when fast magma

ascent results in insufficient time for volatile diffusion into existing bubbles. An increasing supersaturation pressure lowers the critical radius size of bubble embryos and favours bubble nucleation over bubble growth (and/or coalescence) upon decompression (Fiege et al., 2014). Bubble growth in decompressing magma occurs by the diffusion of volatiles from the melt towards the bubble interface, due to the development of concentration gradients of the dissolved volatiles in the melt, and the gas expansion inside the bubble. On the other hand, surface tension and viscous resistance of the surrounding melt hinder bubble growth. The surface tension between basaltic melt and CO_2-dominated bubbles is ~0.36 N/m (Paonita and Martelli, 2006 and references therein). Experimental and theoretical investigations for H_2O-CO_2 mixtures also suggest that CO_2 lowers the surface tension of H_2O-bearing silicic melts (Paonita and Martelli, 2006 and references therein). Yamada et al. (2015) applied the classical nucleation theory to the nucleation of bubbles in the H_2O-CO_2 mixture to observe that the CO_2 content may slightly decreases the surface tension. However, the effect of CO_2 on the surface tension is less effective when the bubble nucleation rate decreases in the vicinity of larger bubbles, as a consequence of the decrease in the volatile

concentration surrounding the growing bubbles (Yamada et al., 2015). For homogeneous bubble nucleation in H_2O+CO_2-bearing systems, the supersaturation pressure increases with decreasing concentration of H_2O and increasing concentration of CO_2, responding mostly to the different pressure dependencies of H_2O and CO_2 solubility in the melt (Mourtada-Bonnefoi and Laporte, 2002). However, for basaltic liquids, no significant effects on the supersaturation pressure are observed at CO_2 concentrations within few hundreds ppm, whereas these effects become noticeable at concentration higher than 0.8 wt% (Bai et al., 2008). Additionally, basaltic melts characterized by lower viscosities are likely to exhibit lower bubble number density at faster growth and coalescence rates, compared to more evolved melts characterized by higher viscosities (cf. Masotta et al., 2014).

H_2O and CO_2 behaviour

The concentrations of H_2O and CO_2 dissolved in the decompressed glasses have been measured for most of the run products, with the exception of CO_2 contents in runs decompressed at 0.01 MPa/s because concentrations were too low (Figure 2).

The concentration of H_2O dissolved in the melt from the run product charged with 1 wt% H_2O + 0.0 wt% CO_2 closely corresponds to the overall H_2O content added to the system (Figure 2). Therefore, it is expected that the relatively low bubble formation in virtually CO_2-absent run products (Figure 1) results from the entrapment of atmospheric nitrogen in the free volume between grains during loading of the powder into the capsule (Botcharnikov et al., 2005).

At the fast decompression rate of 1 MPa/s, the original H_2O concentration is preferentially retained in the melt irrespective of the amount of CO_2 added to the system (Figure 2). This supersaturation condition is more clearly observable for experimental runs charged with 3 wt% H_2O, accounting for the higher volatile content and, consequently, the higher volatile concentration gradients at the bubble-melt interface (Bai et al., 2008). Through the recent thermodynamically-based equation of state proposed by Duan (2014), it has been estimated the equilibrium solubility of H_2O and CO_2 in the trachybasaltic melt at the final pressure of 50 MPa (Figure 3). One of the advantages of this model consists of its applicability over a wide range of pressures (0.0001-0.3 GPa), temperatures (660-1,730), and melt compositions (from ultramafic to silicic, from metaluminous to peraluminous, and from subalkaline to peralkaline) that are not adequately reproduced by previous equations (cf. Duan, 2014). Indeed, the maximum deviation between the H_2O-CO_2 solubility predicted by the model and that measured in laboratory has been tested to be 20% (Duan,
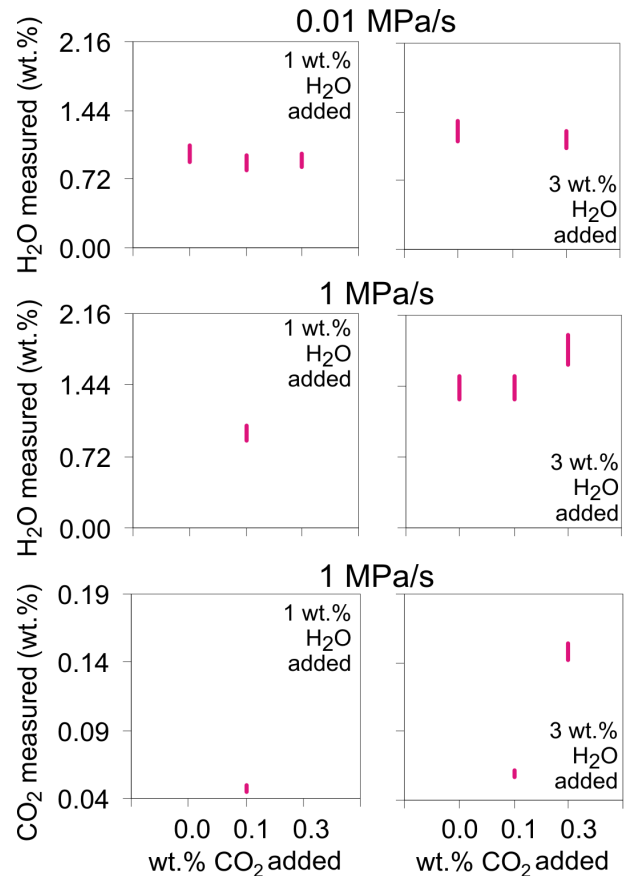
Figure 2. Contents of H_2O and CO_2 dissolved in the decompressed glasses have been measured for most of the run products, with the exception of CO_2 contents in runs decompressed at 0.01 MPa/s because concentrations were too low. The content of H_2O dissolved in the melt from the run product charged with 1 wt% H_2O+0.0 wt% CO_2 closely corresponds to the overall H_2O content added to the system. At the fast decompression rate of 1 MPa/s, the original H_2O concentration is preferentially retained in the melt irrespective of the amount of CO_2 added to the system. This supersaturation condition is more clearly observable for experimental runs charged with 3 wt% H_2O.

2014). In the present study, it has been also calculated the deviation between H_2O-CO_2 solubilities predicted at the final pressure conditions of the experiments and those measured in the quenched glasses. The deviation for H_2O concentrations (ΔH_2O) dissolved in the trachybasaltic melts decompressed at 1 MPa/s is ΔH_2O=0-15% at 1 wt% H_2O but slightly increases to ΔH_2O=4-22% at 3 wt% H_2O (Figure 3). In contrast, the relative deviation to measured CO_2 concentrations (ΔCO_2) is always higher than ΔH_2O, corresponding to ΔCO_2=77-79% at 1 wt% H_2O and ΔCO_2=98-99% at 3 wt% H_2O (Figure 3). This points out that, during melt decompression, CO_2 degassing is less efficient with respect to H_2O transfer from the melt into the
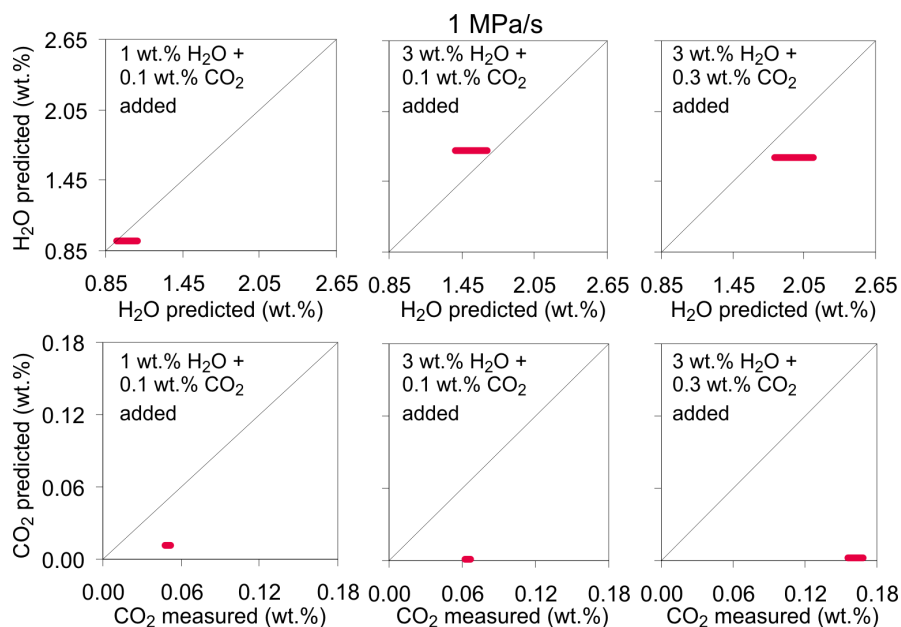
Figure 3. Comparison between H_2O and CO_2 concentrations measured in runs decompressed at 1 MPa/s and the equilibrium solubility of H_2O and CO_2 in the trachybasaltic melt predicted at the final pressure of 50 MPa by the thermodynamically-based equation of state of Duan (2014).

vapor phase. Equilibrium and disequilibrium degassing processes are controlled by the diffusivities of H_2O and CO_2 in the melt and experimental durations. Equilibrium degassing takes place when the gas interface distance (i.e., the distance between two coexisting bubbles) is shorter than diffusion distances for both H_2O and CO_2 (Pichavant et al., 2013). In contrast, disequilibrium degassing takes place (and CO_2-oversaturated melts are produced) when the gas interface distance is longer than the diffusion distance for CO_2 as the slowest diffusing volatile (see discussion below).

In other words, when pressure drops during magma ascent in the volcanic conduit, the trachybasaltic melt can potentially approach the surface being preferentially supersaturated in CO_2. Modeling data from Paonita and Martelli (2013) derived for basaltic systems indicate that ascending magma reaches the surface rather supersaturated in dissolved carbon (supersaturation up to 3.5 times). Therefore, a rising magma can display clear signals of non-equilibrium degassing of dissolved volatiles, such as CO_2 supersaturation in melt and kinetic fractionation. The extent of kinetic disequilibrium is strictly linked to the ascent rate of magmas through the crust. It is interesting that Paonita and Martelli (2013) estimate that CO_2 supersaturation takes place at magma ascent velocities 0.01–10 m/s that are of the same order of magnitude of the experimental ones used in this study. This confirms that, even at relatively slow ascent rates, rising magmas may erupt with significant CO_2 supersaturation under

the effect of a multicomponent H_2O-CO_2 volatile phase. A similar result comes from continuous decompression experiments on a Strombolian basalt (with dissolved H_2O and CO_2 concentrations of 2.7-3.8 wt% and 0.06-0.13 wt%, respectively) kept at a near-liquidus temperature of 1,150 °C and decompressed from 250 MPa down to 25 MPa (Pichavant et al., 2013), in order to simulate natural magma ascent velocities of 0.25-1.50 m/s (Vetere et al., 2007). The inhibited bubble growth at 1 MPa/s causes the formation of relatively small gas bubbles (Figure 1). Under such circumstances, the diffusive motion of volatiles in the melt plays a major role in controlling H_2O and CO_2 loss at the gas-melt interface. Thus, H_2O and CO_2 concentrations in post-decompression glasses may not approach their equilibrium solubilities (Figure 3). Since H_2O diffuses faster than CO_2 in hydrous basaltic melts (up to 10 times faster; Zhang and Stolper 1991), the degassing behaviour of H_2O and CO_2 results to be decoupled, reflecting the difference in melt diffusivity between the two volatile components and causing a disequilibrium degassing trend (Mangan and Sisson 2000).
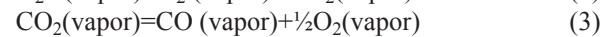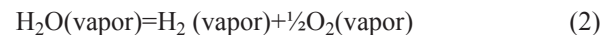
Melt redox state

The measured Fe^{2+}/Fe^{3+} ratios of the decompressed glasses can be used to calculate the redox conditions of the melt during disequilibrium degassing (Table 1S). These estimates have been performed by the equation of Kress and Carmichael (1991) based on T and melt composition. The standard errors of FeO (0.21 wt%) and Fe_2O_3 (0.42
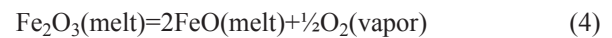
wt%) components used to derive this equation give uncertainty in measured fO_2 of 0.86 log units. We have also determined how error propagates in fO_2 estimates, considering as major source of uncertainty for the equation of Kress and Carmichael (1991) the error of Fe^{2+}/Fe^{3+} ratios and the standard error from replicate microprobe glass analyses (Table 1S). Within the analytical error of the calculated fO_2, the redox state of the system does not show substantial variations, remaining almost close to the QFM buffer (Figure 4). The calculated values of fO_2 are those imposed by the experimental device and fall within the uncertainty of the model proposed by Kress and Carmichael (1991), being in agreement with the reducing conditions estimated for the natural trachybasalt (Lanzafame et al., 2013). Therefore, the variable H_2O-CO_2 concentrations and the different decompression paths do not appear to have any systematic effect on the final redox conditions of the melts that, in turn, remain buffered to the original fO_2 of natural magma upon the effect of disequilibrium degassing. This result clearly contrasts with open-system degassing conditions, such as those responsible for the post-eruptive oxidation of lavas, in which the volatile loss and fractionation of volatile species in the magma exert a dominant control on the final compositions of escaping gases and the redox states of residual melts (e.g., Christie

Figure 4. The measured Fe^{2+}/Fe^{3+} ratios of the decompressed glasses have been used to calculate the redox conditions of the melt during disequilibrium degassing. These estimates have been performed by the equation of Kress and Carmichael (1991) based on T and melt composition. Within the analytical error of the calculated fO_2, the redox state of the system does not show substantial variations, remaining almost close to the QFM buffer.

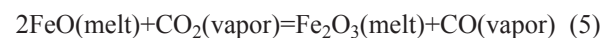et al., 1986; Mollo et al., 2013).

Moore et al. (1995) reported that there is no significant effect of dissolved water on the Fe^{2+}/Fe^{3+} ratio in a peralkaline rhyolite, andesite, and augite minette at H_2O-saturated conditions, P=50-200 MPa, T=950-1,100 °C, and fO_2=NNO+1-NNO+2 (where NNO is the nickel-nickel oxide solid oxygen buffer). In a more recent study by Botcharnikov et al. (2005) conducted on a ferrobasaltic melt equilibrated at P=200 MPa, T=1,200 °C, fO_2=QFM+1-QFM+4.2, and H_2O=0.72-4.67, it has been documented that fO_2 remains the most important factor controlling the oxidation state of iron in silicate melts, whereas the presence of H_2O as a chemical component of the melt at constant T, P, and fO_2 has a small or insignificant influence on the melt Fe^{2+}/Fe^{3+} ratio. However, the authors evidenced as the presence of H_2O in fluid-saturated conditions may indeed be important since aH_2O controls the redox state of the system and, hence, the Fe^{2+}/Fe^{3+} ratio of the melt. Both H_2O and CO_2 are partly decomposed and release oxygen, acting as strong oxidizers for the melt:

$$H_2O(vapor)=H_2 (vapor)+\tfrac{1}{2}O_2(vapor) \qquad (2)$$
$$CO_2(vapor)=CO (vapor)+\tfrac{1}{2}O_2(vapor) \qquad (3)$$

The redox evolution of a degassing magma rising to the surface is also dictated by the initial amount of dissolved iron oxides:

$$Fe_2O_3(melt)=2FeO(melt)+\tfrac{1}{2}O_2(vapor) \qquad (4)$$

While equation (4) is able to weakly buffer the changes in fO_2 during degassing of Fe-poor rhyolitic melts, the buffering capacity of iron species is much higher in Fe-rich liquids such as basalts (Burgisser and Scaillet, 2007). Indeed, if the bulk fluid/melt ratio is relatively low, the Fe^{2+}/Fe^{3+} ratio of the melt can buffer the value of fO_2. In our disequilibrium degassing experiments, the physicochemical state of the system changes from vapor-undersaturated to vapor-saturated conditions at which bubbles nucleate and the transfer of volatiles out of the melt occurs at the gas-melt interface (diffusive volatile transfer). Previous decompression studies on magmatic melt oxidation documented as near the bubble surface, the value of fO2 can locally increase (e.g., Simakin et al., 2012):

$$2FeO(melt)+CO_2(vapor)=Fe_2O_3(melt)+CO(vapor) \quad (5)$$

However, CO and CO_2 have low solubility in the melt and this characteristic may induce local non-equilibrium oxidation far from the bubble surface where volatile concentrations higher than equilibrium values may
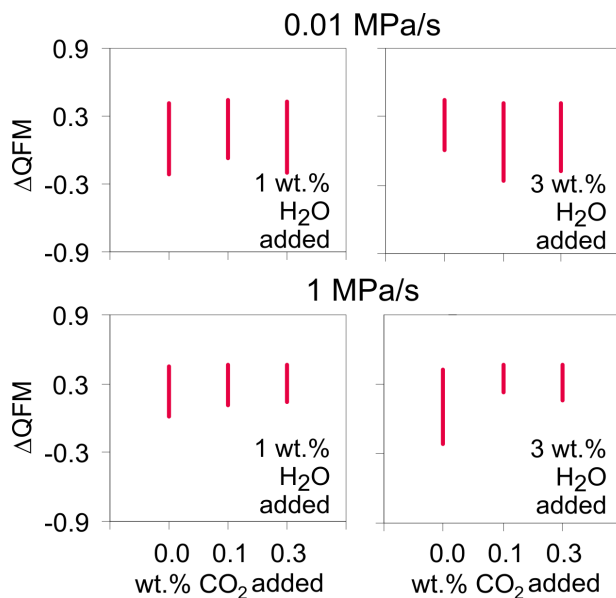
persist in the melt (Pichavant et al., 2013). In contrast, in the presence of H_2O, the fast diffusion of H_2 in the melt can likely counterbalance the oxidative capacity of CO_2 (Simakin et al., 2012):

$$Fe_2O_3(melt)+H_2(vapor)=2FeO(melt)+H_2O(vapor) \quad (6)$$

Considering the rival effects of equation (5) and (6), the value of fO_2 in the decompressed melt may locally change or not during bubble nucleation and growth. Because of the low fluid/melt ratio in our decompression experiments, it is apparent that the bulk melt composition remains buffered to its original redox state, paralleling a number of observations from geochemical and petrological investigations on the behaviour of C-O-H species in degassing lavas (e.g., Gerlach, 1993; Lange and Carmichael, 1996; Kelley and Cottrell, 2009, 2012; Crabtree and Lange, 2012; Brounce et al., 2014; Grocke et al., 2016). These studies demonstrated as the redox equilibrium between Fe^{2+} and Fe^{3+} is inextricably linked to the original redox state of magma. For example, gases collected along the east rift zone of Kilauea (Hawaii, USA), over a temperature interval of 935-1,185 °C, were observed to have a constant value of fO_2 (Gerlach, 1993). Within an error of ± 0.5 log units, the redox state of measured gases was identical to that of the magma feeding Kilauean lava flows, suggesting as fO_2 of exsolved gases is strictly controlled by that of the host magma (Gerlach, 1993). Similarly, thermodynamic calculations conducted on a suite of lava flows from the Aurora volcanic field (California-Nevada, USA) showed that the bulk redox state of the melt does not change even after substantial closed-system degassing and cooling (Lange and Carmichael, 1996). More recent studies on Fe oxidation state in olivine-hosted melt inclusions from Mariana arc basalts showed no systematic change with extent of H_2O degassing (Kelley and Cottrell, 2009, 2012; Brounce et al., 2014). The comparison of pre-eruptive Fe^{2+} concentrations in hydrous andesite and dacite magmas during phenocryst growth with analyses of post-eruptive Fe^{2+} concentrations after degassing evidenced no detectable changes (Crabtree and Lange, 2012; Grocke et al., 2016).

Melt composition

Within the error of ten microprobe analyses, undegassed and degassed glasses show identical concentrations for the non-volatile chemical species expressed as major oxide components (Table 1S). A similar result is also found for measurements of REE, HFSE, LILE, and TE from five replicate laser ablation analyses (Table 1S). The only exceptions are some volatile chemical species (i.e., Cl for halogens, and Li and B for LLE) whose concentrations

in the degassed (bubble-rich) glasses decreases by ~10-50% with respect to those measured in the undegassed (bubble-free) glass (Figure 5). No compositional changes are measured for S and F due to their low initial concentrations (i.e., close to the detection limit of the microprobe analysis). Significant variations of Cl, Li, and B are measured for experiments with 3 wt% H_2O, whereas no appreciable variations are measured for the run products charged with 1 wt% H_2O. The percentage of decrease of volatile chemical species is comparable either when the experimental runs are decompressed at 0.01 MPa/s or at 1 MPa/s. The effect of CO_2 (and fluid speciation) on LLE contents in the degassed glasses seems also to be negligible at the relatively low volatile concentrations used for the decompression experiments (Figure 5). Moreover, CO_2 degassing is less efficient with respect to H_2O (Figure 3). Therefore, H_2O is likely the major volatile component carrying and stabilizing LLE in the fluid. Despite only the initial melt-H_2O content appears to influence the element degassing, the total amount of volatiles added to the experimental charges is between one to two orders of magnitude lower than that of the powdered rock (i.e., the fluid/melt ratio is in the range of ~0.002-0.02). This implies that the initial volatile content is not enough to produce appreciable compositional changes in the melt and the analytical measurements result in errors that are too large to investigate the partitioning of volatile chemical species between the degassed trachybasaltic melt and the vapor.

During decompression from 400 to 50 MPa, the amount of Cl dissolved in the trachybasaltic melt decreases up to ~50% (Figure 5). When Cl is lost from melt into the vapor, most of the degassing process occurs at relatively low pressures (much lower than 100 MPa), regardless of whether the melt is initially saturated or under-saturated in Cl (Gardner et al., 2006; Stelling et al., 2008; Lukanin, 2016). Alletti et al. (2009) investigated the equilibrium partitioning of Cl between a basaltic melt from Mt. Etna volcano and H_2O and H_2O+CO_2 fluids at pressures between 1 and 200 MPa. The authors found that, as the pressure decreases from 200 to 50 MPa, Cl is preferentially partitioned into the vapor phase and its concentration in the melt decreases by ~90% for initial Cl concentration in the melt ≤0.4 wt%. However, under disequilibrium degassing conditions, the gas does not efficiently escape from the melt causing that Cl is poorly extracted from the silicate liquid (Gardner et al., 2006).

Despite Li and B are present in basaltic magmas in low concentrations, their geochemical behaviour in fluid-melt systems has been investigated for both highly silicic (Pichavant, 1981; London et al., 1988; Webster et al., 1989; Schatz et al., 2004) and basaltic (Hervig et al., 2002; Edmonds, 2015) compositions. LLE abundances in
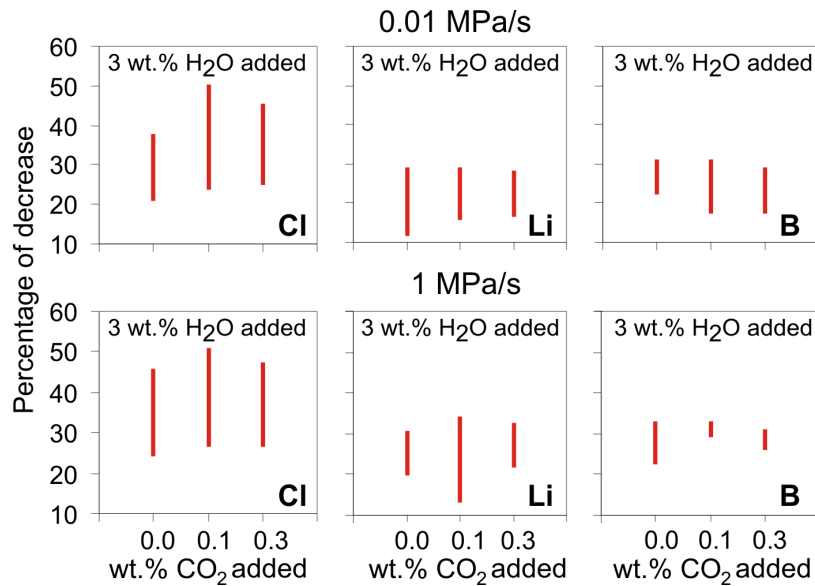
Figure 5. Percentage of decrease of volatile chemical species (i.e., Cl for halogens, and Li and B for LLE) in the degassed (bubble-rich) glasses with respect to concentrations measured in the undegassed (bubble-free) glass. Significant variations of Cl, Li, and B are measured only for experiments with 3 wt% H_2O, whereas no appreciable variations are measured for the run products charged with 1 wt% H_2O. The percentage of decrease of volatile chemical species is comparable either when the experimental runs are decompressed at 0.01 MPa/s or at 1 MPa/s. The amount of CO_2 (and fluid speciation) on LEE contents seems also to be negligible at the relatively low volatile concentrations used for the decompression experiments.

the mantle are influenced by the subduction of sediments inducing heterogeneity both in abundance and in isotopic composition (Kobayashi et al., 2004). Li and B are key tracers for understanding geochemical cycling at magmatic arc settings, as they behave like volatile elements during devolatilization reactions at high pressures (Moriguti et al., 2004). Li and B are weakly partition into minerals crystallizing from silicate melts (Herd et al., 2004), which allows for an observable record of melt LEE contents to be preserved in crystals. Through an indirect geochemical method based on volatile and trace element equilibrium concentrations in olivine-hosted melt inclusions from basaltic eruptions at Kilauea volcano, Edmonds (2015) has observed that LLE decreases by ~20-50% with decreasing H_2O. Looking at the decompression experiments from this study (and considering the analytical uncertainty of replicate laser ablation analyses), LLE are also found to decrease by ~10-32% (Table 1S). The good match between our data and those from Edmonds (2015) confirms that, at relative lo pressure conditions, LLE may be incorporated into a hydrous vapor during H_2O exsolution from the melt. This evidence suggests that Li and B can be considered as effective tracers of degassing processes during magma ascent and eruption (Whitworth and Rankin, 1989; Webster et al., 1996; Vlastélic et al., 2011), as well as during lava flowage onto the surface (Kuritani and Nakamura, 2006; Mollo et al., 2013).

CONCLUDING REMARKS

We performed disequilibrium decompression experiments using as starting melt a H_2O+CO_2-bearing trachybasalt from Mt. Etna volcano, in order to investigate the change in abundances of volatile components in the melt during slow and fast magma ascent conditions. The following main conclusions can be drawn:

H_2O supersaturation does not occur in the melt when the initial H_2O content is 1 wt%;

The minimum threshold to observe supersaturation at the fast decompression rate of 1 MPa/s corresponds to an initial H_2O content between 1 and 3 wt%;

CO_2 degassing is less efficient with respect to H_2O transfer from the melt into the vapor phase;

The trachybasaltic melt is preferentially supersaturated in CO_2 with decreasing pressure;

The bulk melt remains buffered to its original redox state upon disequilibrium degassing conditions;

Significant devolatilization of Cl, Li, and B is measured only when the initial H_2O content is 3 wt% (i.e., a larger amount of fluid compared to experiments charged with 1 wt% H_2O), and no appreciable variations are measured as a function of CO_2 content and decompression path investigated in this study.

REFERENCES

Alletti M., Baker D.R., Scaillet B., Aiuppa A., Moretti R., Ottolini L., 2009. Chlorine partitioning between a basaltic melt and H_2O-CO_2 fluids at Mount Etna. Chemical Geology 263, 37-50.

Aloisi M., Bonaccorso A., Gambino S., 2006. Imaging composite dike propagation (Etna, 2002 case). Journal of Geophysical Research: Solid Earth 111, n/a-n/a.

Armienti P., Perinelli C., Putirka K.D., 2013. A new model to estimate deep-level magma ascent rates, with applications to Mt. Etna (Sicily, Italy). Journal of Petrology 54, 795-813.

Bai L., Baker D.R., Rivers M., 2008. Experimental study of bubble growth in Stromboli basalt melts at 1 atm. Earth and Planetary Science Letters 267, 533-547.

Berndt J., Liebske C., Holtz F., Freise M., Nowak M., Ziegenbein D., Hurkuck W., Koepke J., 2002. A combined rapid-quench and H_2-membrane setup for internally heated pressure vessels: description and application for water solubility in basaltic melts. American Mineralogist 87, 1717-1726.

Blower J.D., Keating J.P., Mader H.M., Phillips J.C., 2001. Inferring volcanic degassing processes from vesicle size distributions. Geophysical Research Letters 28, 347-350.

Botcharnikov R.E., Almeev R.R., Koepke J., Holtz F., 2008. Phase relations and liquid lines of descent in hydrous ferrobasalt - Implications for the Skaergaard intrusion and Columbia river flood basalts. Journal of Petrology 49, 1687-1727.

Botcharnikov R.E., Koepke J., Holtz F., McCammon C., Wilke M., 2005. The effect of water activity on the oxidation and structural state of Fe in a ferro-basaltic melt. Geochimica et Cosmochimica Acta 69, 5071-5085.

Brounce M.N., Kelley K.A., Cottrell E., 2014. Variations in Fe^{3+}/$\sum Fe$ of Mariana arc basalts and mantle wedge fO_2. Journal of Petrology 55, 2513-2536.

Brugger C.R. and Hammer J.E., 2010. Crystallization kinetics in continuous decompression experiments: Implications for interpreting natural magma ascent processes. Journal of Petrology 51, 1941-1965.

Burgisser A. and Gardner J.E., 2004. Experimental constraints on degassing and permeability in volcanic conduit flow. Bulletin of Volcanology 67, 42-56.

Burgisser A. and Scaillet B., 2007. Redox evolution of a degassing magma rising to the surface. Nature 445, 194-197.

Christie D.M., Carmichael I.S.E., Langmuir C.H., 1986. Oxidation states of mid-ocean ridge basalt glasses. Earth and Planetary Science Letters 79, 397-411.

Collins S.J., Pyle D.M., Maclennan J., 2009. Melt inclusions track pre-eruption storage and dehydration of magmas at Etna. Geology 37, 571-574.

Crabtree S.M. and Lange R.A., 2012. An evaluation of the effect of degassing on the oxidation state of hydrous andesite and dacite magmas: a comparison of pre- and post-eruptive Fe^{2+} concentrations. Contributions to Mineralogy and Petrology 163, 209-224.

Demouchy S., Jacobsen S.D., Gaillard F., Stem C.R., 2006. Rapid magma ascent recorded by water diffusion profiles in mantle olivine. Geology 34, 429-432.

Dixon J.E., Pan V., 1995. Determination of the molar absorptivity of dissolved carbonate in basanitic glass. American Mineralogist 80, 1339-1342.

Dixon J.E., Stolper E.M., Holloway J.R., 1995. An experimental study of water and carbon dioxide solubilities in mid-ocean ridge basaltic liquids. Part I: calibration and solubility models. Journal of Petrology 36, 1607-1631.

Duan X., 2014. A general model for predicting the solubility behavior of H_2O-CO_2 fluids in silicate melts over a wide range of pressure, temperature and compositions. Geochimica et Cosmochimica Acta 125, 582-609.

Duffell H.J., Oppenheimer C., Pyle D.M., Galle B., McGonigle A.J.S., Burton M.R., 2003. Changes in gas composition prior to a minor explosive eruption at Masaya volcano, Nicaragua. Journal of Volcanology and Geothermal Research 126, 327-339.

Edmonds M., 2015. Partitioning of light lithophile elements during basalt eruptions on Earth and application to Martian shergottites. Earth and Planetary Science Letters 411, 142-150.

Fiege A. and Cichy S.B., 2015. Experimental constraints on bubble formation and growth during magma ascent: a review. American Mineralogist 100, 2426-2442.

Fiege A., Holtz F., Cichy S.B., 2014. Bubble formation during decompression of andesitic melts. American Mineralogist 99, 1052-1062.

Gardner J.E., Burgisser A., Hort M., 2006. Experimental and model constraints on degassing of magma during ascent and eruption. Geological Society of America Special Papers 402, 99-113.

Gerlach T.M., 1993. Oxygen buffering of Kilauea volcanic gases and the oxygen fugacity of Kilauea basalt. Geochimica et Cosmochimica Acta 57, 795-814.

Gonnermann H., Manga M., 2012. Dynamics of magma ascent in the volcanic conduit. In: Modeling Volcanic Processes: The Physics and Mathematics of Volcanism. (eds): S.A. Fagents, T.K.P. Gregg and R.M.C. Lopes, Cambridge University Press, Cambridge, 55-84.

Grocke S.B., Cottrell E., de Silva S., Kelley K.A., 2016. The role of crustal and eruptive processes versus source variations in controlling the oxidation state of iron in Central Andean

magmas. Earth and Planetary Science Letters 440, 92-104.

Herd C.D.K., Treiman A.H., McKay G.A., Shearer C.K., 2004. The behaviour of Li and B during planetary basalt crystallization. American Mineralogist 89, 832-840.

Hervig R.L., Moore G.M., Williams L.B., Peacock S.M., Holloway J.R., Roggensack K., 2002. Isotopic and elemental partitioning of boron between hydrous fluid and silicate melt. American Mineralogist 87, 769-774.

Hildner E., Klügel A., Hauff F., 2011. Magma storage and ascent during the 1995 eruption of Fogo, Cape Verde Archipelago. Contributions to Mineralogy and Petrology 162, 751-772.

Kelley K.A. and Cottrell E., 2009. Water and the oxidation state of subduction zone magmas. Science 325, 605-607.

Kelley K.A. and Cottrell E., 2012. The influence of magmatic differentiation on the oxidation state of Fe in a basaltic arc magma. Earth and Planetary Science Letters 329-330, 109-121.

Kobayashi K., Tanaka R., Moriguti T., Shimizu K., Nakamura E., 2004. Lithium, boron, and lead isotope systematics of glass inclusions in olivines from Hawaiian lavas: evidence for recycled components in the Hawaiian plume. Chemical Geology 212, 143-161.

Kress V.C. and Carmichael I.S.E., 1991. The compressibility of silicate liquids containing Fe_2O_3 and the effect of composition, temperature, oxygen fugacity and pressure on their redox states. Contributions to Mineralogy and Petrology 108, 82-92.

Kuritani T. and Nakamura E., 2006. Elemental fractionation in lavas during post-eruptive degassing: evidence from trachytic lavas, Rishiri Volcano, Japan. Journal of Volcanology and Geothermal Research 149, 124-138.

Lange R.A. and Carmichael I.S.E., 1996. The Aurora volcanic field, California-Nevada: oxygen fugacity constraints on the development of andesitic magma. Contributions to Mineralogy and Petrology 125, 167-185.

Lanzafame G., Mollo S., Iezzi G., Ferlito C., Ventura G., 2013. Unraveling the solidification path of a pahoehoe "cicirara" lava from Mount Etna volcano. Bulletin of Volcanology 75, 1-16.

Lesne P., Kohn S.C., Blundy J., Witham F., Botcharnikov R.E., Behrens H., 2011. Experimental simulation of closed-system degassing in the system basalt-H_2O-CO_2-S-Cl. Journal of Petrology 52, 1737-1762.

London D., Hervig R.L., Morgan G.B., 1988. Melt-vapor solubilities and elemental partitioning in peraluminous granite-pegmatite systems: experimental results with Macusani glass at 200 MPa. Contributions to Mineralogy and Petrology 99, 360-373.

Lukanin O.A., 2016. Chlorine partitioning between melt and aqueous chloride fluid phase during granite magma degassing. Part II. Crystallization-induced degassing of melts. Geochemistry International 54, 660-680.

Mangan M. and Sisson T., 2000. Delayed, disequilibrium degassing in rhyolite magma: decompression experiments and implications for explosive volcanism. Earth and Planetary Science Letters 183, 441-455.

Marxer H., Bellucci P., Nowak M., 2015. Degassing of H_2O in a phonolitic melt: a closer look at decompression experiments. Journal of Volcanology and Geothermal Research 297, 109-124.

Masotta M., Ni H., Keppler H., 2014. In situ observations of bubble growth in basaltic, andesitic and rhyodacitic melts. Contributions to Mineralogy and Petrology 167, 1-14.

Mollo S., Giacomoni P.P,., Coltorti M., Ferlito C, Iezzi G., Scarlato P., 2015a. Reconstruction of magmatic variables governing recent Etnean eruptions: constraints from mineral chemistry and P-T-fO_2-H_2O modelling. Lithos 212-215, 311-320, 10.1016/j.lithos.2014.11.020.

Mollo S., Giacomoni P.P., Andronico D., Scarlato P., 2015b. Clinopyroxene and titanomagnetite cation redistributions at Mt. Etna volcano (Sicily, Italy): Footprints of the final solidification history of lava fountains and lava flows. Chemical Geology 406, 45-54, http://dx.doi.org/10.1016/j.chemgeo.2015.04.017.

Mollo S., Scarlato P., Lanzafame G., Ferlito C., 2013. Deciphering lava flow post-eruption differentiation processes by means of geochemical and isotopic variations: A case study from Mt. Etna volcano. Lithos 162-163, 115-127, http://dx.doi.org/10.1016/j.lithos.2012.12.020.

Moore G., Vennemann T., Carmichael, I.S.E., 1995. Solubility of water in magmas to 2 kbar. Geology 23, 1099-1102.

Moriguti T., Shibata T., Nakamura E., 2004. Lithium, boron and lead isotope and trace element systematics of Quaternary basaltic volcanic rocks in northeastern Japan: mineralogical controls on slab-derived fluid composition. Chemical Geology 212, 81-100.

Mourtada-Bonnefoi C.C. and Laporte D., 2002. Homogeneous bubble nucleation in rhyolitic magmas: an experimental study of the effect of H_2O and CO_2. Journal of Geophysical Research: Solid Earth 107, ECV 2-1-ECV 2-19.

Nowak M., Cichy S.B., Botcharnikov R.E., Walker N., Hurkuck W., 2011. A new type of high-pressure low-flow metering valve for continuous decompression: first experimental results on degassing of rhyodacitic melts. American Mineralogist 96, 1373-1380.

Ohlhorst S., Behrens H., Holtz F., 2001. Compositional dependence of molar absorptivities of near-infrared OH^- and H_2O bands in rhyolitic to basaltic glasses. Chemical Geology 174, 5-20.

Paonita A. and Martelli M., 2006. Magma dynamics at mid-ocean ridges by noble gas kinetic fractionation: Assessment of magmatic ascent rates. Earth and Planetary Science Letters 241, 138-158.

Perinelli C., Mollo S., Gaeta M., De Cristofaro S.P., Palladino D.M., Armienti P., Scarlato P., Putirka K.D., 2016. An improved clinopyroxene-based hygrometer for Etnean magmas and implications for eruption triggering mechanisms.

American Mineralogist 101, 2774-2777, doi: 10.2138/am-2016-5916.

Pichavant M., 1981. An experimental study of the effect of boron on a water saturated haplogranite at 1 kbar vapour pressure. Contributions to Mineralogy and Petrology 76, 430-439.

Pichavant M., Di Carlo I., Rotolo S.G., Scaillet B., Burgisser A., Le Gall N., Martel C., 2013. Generation of CO_2-rich melts during basalt magma ascent and degassing. Contributions to Mineralogy and Petrology 166, 545-561.

Preuss O., Marxer H., Ulmer S., Johannes W., Nowak M., 2016. Degassing of hydrous trachytic Campi Flegrei and phonolitic Vesuvius melts: experimental limitations and chances to study homogeneous bubble nucleation. American Mineralogist 101, 859-875.

Rutherford M.J., 2008. Magma ascent rates. Reviews in Mineralogy and Geochemistry 69, 241-271.

Rutherford M.J. and Hill P.M., 1993. Magma ascent rates from amphibole breakdown: an experimental study applied to the 1980-1986 Mount St. Helens eruptions. Journal of Geophysical Research 98, 667-685.

Schatz O.J., Dolejš D., Stix J., Williams-Jones A.E., Layne G.D., 2004. Partitioning of boron among melt, brine and vapor in the system haplogranite-H_2O-NaCl at 800 °C and 100 MPa. Chemical Geology 210, 135-147.

Schuessler J.A., Botcharnikov R.E., Behrens H., Misiti V., Freda C., 2008. Amorphous materials: properties, structure, and durability: oxidation state of iron in hydrous phono-tephritic melts. American Mineralogist 93, 1493-1504.

Simakin A.G., Salova T.P., Bondarenko G.V., 2012. Experimental study of magmatic melt oxidation by CO_2. Petrology 20, 593-606.

Spilliaert N., Allard P., Métrich N., Sobolev A.V., 2006. Melt inclusion record of the conditions of ascent, degassing, and extrusion of volatile-rich alkali basalt during the powerful 2002 flank eruption of Mount Etna (Italy). Journal of Geophysical Research: Solid Earth 111, B04203.

Stelling J., Botcharnikov R.E., Beermann O., Nowak M., 2008. Solubility of H_2O- and chlorine-bearing fluids in basaltic melt of Mount Etna at T=1050-1250 °C and P=200 MPa. Chemical Geology 256, 101-109.

Stolper E., 1982. The speciation of water in silicate melts. Geochimica et Cosmochimica Acta 46, 2609-2620.

Symonds R.B., Rose W.I., Bluth G.J.S., Gerlach, T.M., 1994. Volcanic-gas studies: methods, results, and applications. Reviews in Mineralogy and Geochemistry 30, 1-66.

Toramaru A., Noguchi S., Oyoshihara S., Tsune A., 2008. MND (microlite number density) water exsolution rate meter. Journal of Volcanology and Geothermal Research 175, 156-167.

Vetere F., Behrens H., Misiti V., Ventura G., Holtz F., De Rosa R., Deubener J., 2007. The viscosity of shoshonitic melts (Vulcanello Peninsula, Aeolian Islands, Italy): insight on the magma ascent in dikes. Chemical Geology 245, 89-102.

Vetere F., Holtz F., Behrens H., Botcharnikov R.E., Fanara S., 2014. The effect of alkalis and polymerization on the solubility of H_2O and CO_2 in alkali-rich silicate melts. Contributions to Mineralogy and Petrology 167, 1014.

Vlastélic I., Staudacher T., Bachèlery P., Télouk P., Neuville D., Benbakkar M., 2011. Lithium isotope fractionation during magma degassing: constraints from silicic differentiates and natural gas condensates from Piton de la Fournaise volcano (Réunion Island). Chemical Geology 284, 26-34.

Webster J.D., Burt D.M., Aguillon, R.A., 1996. Volatile and lithophile trace-element geochemistry of heterogeneous Mexican tin rhyolite magmas deduced from compositions of melt inclusions. Geochimica et Cosmochimica Acta 60, 3267-3283.

Webster J.D., Holloway J.R., Hervig R.L., 1989. Partitioning of lithophile trace elements between H_2O and H_2O+CO_2 fluids and topaz rhyolite melt. Economic Geology 84, 116-134.

Whitworth M.P. and Rankin A.H., 1989. Evolution of fluid phases associated with lithium pegmatites from SE Ireland. Mineralogical Magazine 53, 271-284.

Yamada K., Tanaka H., Nakazawa K., Emori H., 2005. A new theory of bubble formation in magma. Geophysical Journal Research 110:B02203

Zhang Y. and Stolper E.M., 1991. Water diffusion in a basaltic melt. Nature 351, 306-309.